Oxygen nonstoichiometry and dielectric evolution of $BaTiO_3$. Part I—improvement of insulation resistance with reoxidation

G. Y. Yang, E. C. Dickey, and C. A. Randall
Department of Materials Science and Engineering, Center for Dielectric Studies, and The Materials Research Institute, Pennsylvania State University, University Park, Pennsylvania 16802

D. E. Barber, P. Pinceloup, M. A. Henderson, R. A. Hill, J. J. Beeson, and D. J. Skamser
KEMET Electronics Corporation, 201 Fairview Street Extension, Fountain Inn, South Carolina 29644

(Received 25 May 2004; accepted 1 September 2004)

Impedance spectroscopy, transmission electron microscopy, and electron energy-loss spectroscopy are used to correlate local electrical properties with the microstructure and microchemistry of $BaTiO_3$ in Ni-electrode multilayer ceramic capacitors. High densities of linear defects and some grains with structural modulations are observed in $BaTiO_3$ grains in the as-cofired capacitors. The modulated structure is formed on {111} planes of the $BaTiO_3$. Both types of structural defects are associated with high concentrations of oxygen vacancies. In particular, the oxygen content in the $BaTiO_3$ grains that are in direct contact with the internal Ni electrodes is less uniform with a systematic decrease in oxygen content towards the electrode. In the capacitors that are reoxidized in a higher oxygen partial pressure at lower temperature, the $BaTiO_3$ grains are almost free of linear defects and structural modulations and the oxygen content is homogeneous throughout the $BaTiO_3$ active layers. A concomitant improvement in the total insulation resistance is observed. © *2004 American Institute of Physics*. [DOI: 10.1063/1.1809267]

I. INTRODUCTION

$BaTiO_3$ is the dielectric constituent of commercial multilayer ceramic capacitors (MLCCs) owing to its extremely high dielectric constant associated with a series of ferroelectric phase transitions. MLCCs, in which hundreds of dielectric layers and internal electrodes are alternately stacked, continue to advance in terms of high capacitive volumetric efficiency.[1] An ongoing issue in the performance of these and similar dielectric devices is adequate insulation resistance, which depends sensitively on the oxygen activity during processing and which can degrade under direct-current (dc) bias due to electromigration of charged defects.[2–7] In these types of electroceramic oxides, the local defect chemistries at grain boundaries and electrode interfaces play critical roles in the macroscopic dielectric behavior and degradation kinetics. However, the intimate relationships between local defect chemistry, microstructure, and electrical properties are not well understood.

The major objective of this work is to systematically study electrochemically induced microstructural and microchemical changes in $BaTiO_3$ and their implications for electrical behavior. Since the macroscopic properties of the material are derived from contributions from the $BaTiO_3$ grain interiors, grain boundaries, and electrode interfaces, it is necessary to distinguish these parts of the microstructure both electrically and microchemically. To accomplish this, we utilize complex impedance spectroscopy (IS) and analytical electron microscopy (AEM) in a complementary fashion.

The state-of-the-art base-metal electrode (BME) MLCCs (Refs. 2 and 3) are produced by cofiring doped $BaTiO_3$ with nickel internal electrodes under highly reducing atmospheres (10^{-10}–10^{-12} atm.) at 1250–1300 °C to prevent oxidation of the Ni. The $BaTiO_3$ in the as-cofired MLCC is oxygen deficient, so a subsequent annealing step in a P_{O_2} of $\sim 10^{-8}$ at approximately 800 °C is performed to improve insulation resistance. Part I of this study concentrates on the origins of the insulation resistance improvements that occur during this reoxidation process. The companion Part II paper concerns the details of the microstructural/microchemical changes that occur during electrical degradation under applied dc bias.[8]

II. EXPERIMENTAL PROCEDURES

A. Production of Ni-$BaTiO_3$ MLCCs

In MLCC applications, $BaTiO_3$ is formulated with chemical additives so that the capacitance does not vary by ±15% from the room temperature capacitance between −55 °C and 125 °C. The Ni-$BaTiO_3$ MLCC capacitors are produced following the basic procedures:

(1) Unfired, or green, chips are produced by screen printing Ni paste onto doped $BaTiO_3$ tapes.

(2) The green chips are cofired at ~1300 °C for 2 h in a P_{O_2} of $\sim 10^{-10}$ atm.

(3) The cofired Ni-$BaTiO_3$ MLCCs are then annealed (reoxidized) at ~800 °C for 8 h in a P_{O_2} of $\sim 10^{-8}$ atm.

(4) Termination electrodes are screen printed and post-fired in a N_2 atmosphere. The capacitance of the resulting device is 2.2 μF. The capacitor size is $3.5 \times 2.5 \times 1.15$ mm^3 with Ni electrode thickness of 2 μm and active layer thickness about 12 μm.

B. Impedance spectroscopy

The frequency dependence of the impedance of the co-fired (before reoxidation) and of the as-produced (after reoxidation) capacitors is measured between 10^{-1} and 10^6 Hz over

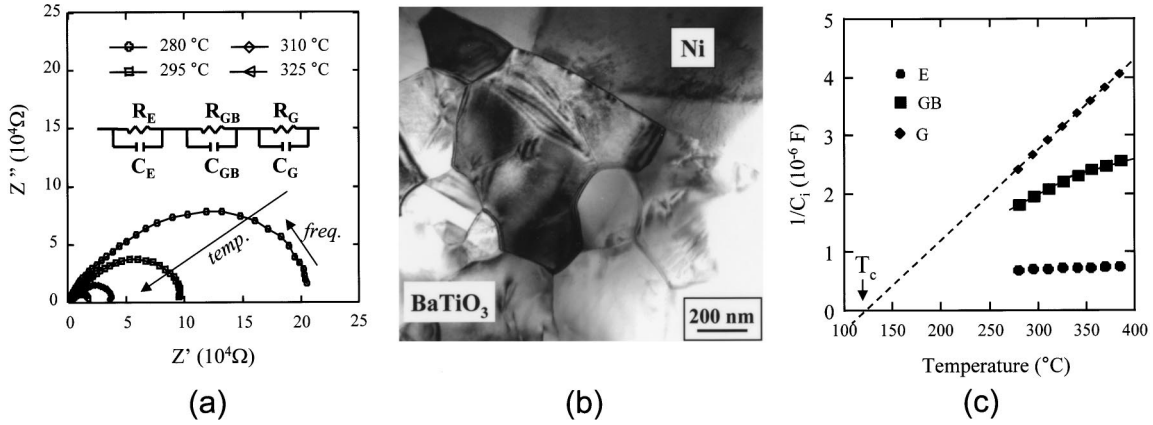

FIG. 1. (a) A series of complex impedance spectroscopy plots of Ni-$BaTiO_3$ multilayer ceramic capacitor. (b) Typical bright-field TEM image of the MLCC. (c) The plot of $1/C_i$ vs T (°C), a linear relationship of $1/C_G$ vs T indicating the ferroelectric nature of $BaTiO_3$.

a temperature range of 265–385 °C using a *Solartron* SI1287 electrochemical interface and 1255B frequency response analyzer with a V_{rms} of 100 mV. The lowest measured temperature is limited by the resistance limit of the instrumentation (1 MΩ). Data are collected under N_2 atmospheres to avoid oxidation of the end copper terminations of the MLCCs; however, the $BaTiO_3$ cannot equilibrate with this external oxygen activity at the test temperatures. Analysis and fitting of the experimental impedance data are accomplished using the electrochemical impedance software, *Z*-plot, and *Z*-view for Windows (*Scribner Associates*). Experimental data are fitted with lumped impedance models based on simple equivalent circuits. The equivalent circuits used for modeling the capacitors consist primarily of ideal parallel resistance-capacitance (RC) elements representing leaky capacitors connected in series.[2] For ferroelectric materials, the temperature dependence of the capacitance assists in identifying the RC values that are from ferroelectric regions of the microstructure. In fact, plots of inverse capacitance versus temperature (i.e., Curie-Weiss behavior) have been used to help validate an equivalent circuit model. Errors are calculated from a least-squares approach of the fitted data.

C. Analytical electron microscopy

AEM is used in a complementary fashion to correlate physical models developed from the IS to the microstructural features of the capacitors. Cross-sectional TEM samples of the Ni-$BaTiO_3$ MLCCs are prepared following traditional procedures including mechanical polishing and ion milling. Ion milling is performed using an EA Fishione Model 3000 ion mill operating at 4–5 kV and 5 mA with an inclination angle of 10°–12°. The samples are cooled with liquid nitrogen during ion milling to minimize structural damage and oxygen vacancy rearrangement. Microstructural and microchemical studies are performed using a JEOL transmission electron microscope equipped with a field emission gun (JEOL 2010F) operating at 200 kV. Electron energy-loss spectroscopy (EELS) is performed with a Gatan Enfina parallel EEL spectrometer attached to the JEOL 2010F microscope. The energy resolution at the zero-loss peak is about 1.1 eV full width at half maximum. EELS are recorded in TEM-diffraction mode with a collection angle of 14 mrad and are analyzed using Gatan DigitalMicrograph software.

D. Scanning electron microscopy–voltage contrast imaging

Scanning electron microscopy–voltage contrast (SEM-VC) imaging is performed using a HITACHI S-3000H scanning electron microscope with an acceleration voltage of 2 kV. A dc field of about 7 V is applied to the as-produced MLCCs to identify highly conductive regions.

III. RESULTS AND DISCUSSIONS

A. Complex impedance spectroscopy

Figure 1(a) shows a set of IS plots of a Ni-$BaTiO_3$ MLCC over a wide range of frequencies at various temperatures. The arrows indicate the directions of increasing frequency and temperature. The shape of the IS plots is far from an ideal semicircle, indirectly indicating that a complicated electrical equivalent circuit for the Ni-$BaTiO_3$ MLCC is needed. In the complex impedance plane, the intercept of the IS plot with the real axis, Z', corresponds to the total resistance of the capacitor.[9–12] As expected, the total resistance of the MLCC decreases with increasing temperature. Figure 1(b) shows a typical bright-field TEM image of an as-produced MLCC. The $BaTiO_3$ grains, $BaTiO_3$ grain boundaries, and Ni-$BaTiO_3$ interfaces are clearly shown. The bright-field TEM image does not reveal a "core-shell" structure for most $BaTiO_3$ grains, which is a typical microstructure for dielectric grains in some X7R $BaTiO_3$ dielectrics.[13–15] Additionally, both grain boundaries and electrode interfaces are free of any additional phases. The impedance of the Ni-$BaTiO_3$ MLCC has contributions from the electrode interfaces, grain boundaries, and $BaTiO_3$ dielectric grains. Thus, an equivalent circuit of three RC elements in series is proposed [see the inset in Fig. 1(a)], where subscript *E* refers the electrode interfaces, GB the grain boundaries, and G the bulk grains. Indeed, the 3*RC* equivalent circuit is sufficient to fit the experimental impedance plots in this work, which indicates that Schottky barriers are formed at

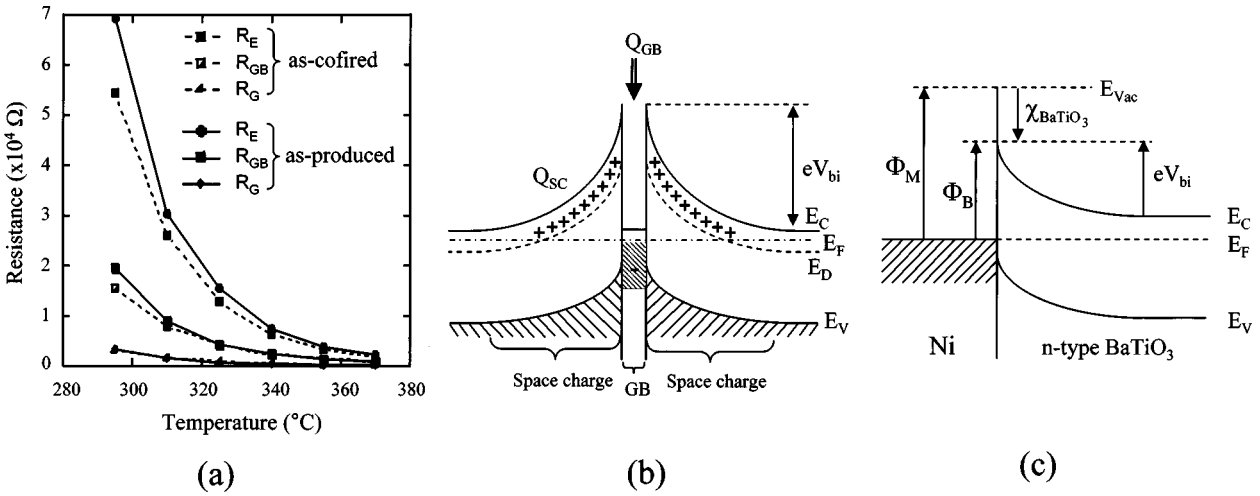

FIG. 2. (a) Resistance variation as a function Ni-$BaTiO_3$ MLCCs states. The contributions from grain boundaries and electrode interfaces play important roles in total insulation resistance of the capacitors. (b) A schematic presentation of a double Schottky barrier at grain boundary. (c) A schematic presentation of the Schottky barrier formed at the interface between the Ni electrode and *n*-type $BaTiO_3$ grains.

the $BaTiO_3$ grain boundaries and Ni/$BaTiO_3$ interfaces.[16,17] The values of resistance and capacitance for each circuit element are obtained by fitting the experimental impedance data with the 3*RC* electrical circuit model.

Although TEM images of the as-cofired capacitors are not shown, the general structure of the MLCC is identical to that observed in the as-produced capacitors. Thus, in this work, the 3*RC* equivalent circuit is used to fit the experimental impedance data for both the cofired and the as-produced MLCCs. The component associated with the bulk grain must follow the Curie-Weiss law. The reciprocal capacitance $(1/C_i)$ for the *i*th circuit element versus temperature T (°C) behaviors is shown in Fig. 1(c). Only one component exhibits a linear relationship of $1/C$ versus T, indicating its ferroelectric nature of

$$C_i \propto \varepsilon_i \propto K/(T - T_C), \tag{1}$$

where ε is the dielectric constant, and K is Curie constant, and T_C is critical temperature for the ferroelectric-paraelectric transition. The circuit element that exhibits Curie-Weiss behavior must be associated with the bulk $BaTiO_3$ grains. The temperature extrapolation for the transition temperature T_C is 123±2 °C for the as-produced capacitors. The circuit elements associated with the grain boundaries and electrode interfaces do not exhibit the Curie-Weiss behavior. The circuit element that does not have a temperature dependence must be associated with Ni-$BaTiO_3$ electrode interfaces (C_E) due to the non-ferroelectric nature of metal-ceramic interfaces.[16,18] The grain boundary capacitance C_{GB} has a complex temperature dependence. The value of $1/C_{GB}$ is nonlinear and the slope decreases in the higher temperature range. The lowering of grain boundary capacitance at higher temperature reflects the decrease in the concentration of the occupied acceptor states, which results in a smaller grain boundary width.[19]

Figure 2(a) shows the resistance of individual circuit elements of the Ni-$BaTiO_3$ MLCCs as a function of temperature. The half-open symbols represent the data obtained from the cofired capacitor (before reoxidation) and the solid symbols represent the data from the as-produced capacitors (after reoxidation). The relationship of $R_E > R_{GB} > R_G$ indicates that the contributions from grain boundaries and electrode interfaces play an important role in the total insulation resistance of the capacitors, which is attributed to the formation of Schottky barriers at grain boundaries and electrode interfaces. The resistances are significantly increased through the reoxidation treatment. It is believed that $BaTiO_3$ is highly oxygen deficient in the cofired capacitors under an oxygen partial pressure of 10^{-10} atm. The reduction reaction produces oxygen vacancies which are the major source of defects in $BaTiO_3$ crystals. Even though the $BaTiO_3$ is formulated with acceptors and amphoteric dopants, the large amount of oxygen vacancies may dominant and through the compensation with electrons makes the material *n* type. This is consistent with the observation that reoxidation increases the insulation resistance in all distributed elements (electrode interface, grain boundaries, and grains).

The formation of double Schottky electrical barriers at grain boundaries is attributed to acceptor and amphoteric doping of the *n*-type $BaTiO_3$ dielectric and segregation of the dopants.[20,21] A double Schottky barrier at grain boundaries, correlated with acceptor segregation, controls conduction of electrons and oxygen vacancies across grain boundaries.[17,22,23] A schematic representation of a double Schottky barrier is given in Fig. 2(b). The $BaTiO_3$ in the current work is doped with several acceptor (e.g., Ca) and amphoteric dopants (e.g., Y). The amphoteric dopants act as donors when occupying the Ba sites or as acceptors when occupying the Ti sites. Earlier studies of amphoteric dopants in bulk $BaTiO_3$ showed that the oxygen vacancies can be buffered in the site changing of an amphoteric dopant.[24] Although originally developed for bulk, similar defect reactions are expected to occur in the grain boundary regions. The occupancy ratio of Y at grain boundaries ($[Y^*_{Ba}]/[Y'_{Ti}]$) in the bulk was found proportional to the concentration of oxygen vacancies $[V^{**}_O]$, and a similar trend could occur at lower temperature in the grain boundaries. The increase in resistance at grain boundaries upon reoxidation results from the

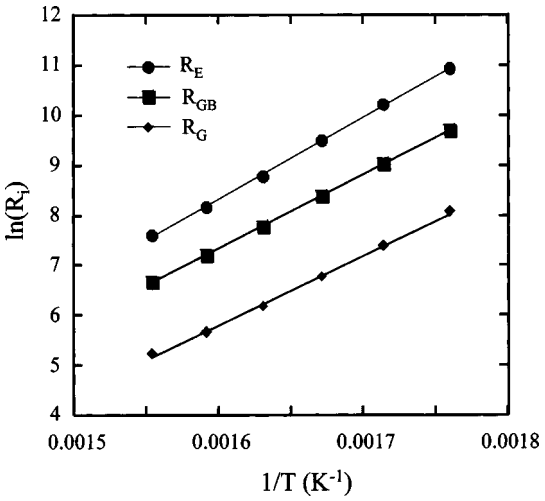

FIG. 3. Typical plots of $\ln(R_i)$ vs $1/T$ of Ni-$BaTiO_3$ MLCC. Activation energies for each circuit element is calculated from the slopes of the plots.

effective increase in net acceptor charges, but loss of oxygen vacancies, and a shift would result in occupancy from *A* site to *B* site.

The Ni-$BaTiO_3$ interface is also a Schottky contact considering the work function of Ni (Φ_{Ni}) to be 5.1 eV and the electron affinity of $BaTiO_3$ (χ_{BaTiO_3}) to be 3.9 eV.[25,26] The Schottky potential barrier eV_{bi} is formed as a result of the band-bending required to accommodate the Fermi energies of the Ni ($E_{F(Ni)}$) and $BaTiO_3$ ($E_{F(BaTiO_3)}$).[27,28] The Schottky barriers at the electrode interfaces control conduction of electrons across electrode interfaces, a schematic representation of the interface barrier with Ni and *n*-type $BaTiO_3$ is shown in Fig. 2(c).

Figure 3 shows the natural log of the resistance versus inverse absolute temperature, which shows that the resistances vary according to an Arrhenius relationship

$$R_i = R_0 \exp(E_{A,i}/kT), \tag{2}$$

where R_0 is a constant, $E_{A,i}$ the activation energy for conduction for the *i*th circuit element, *k* the Boltzmann constant, and *T* absolute temperature. The activation energy of each circuit element is listed in Table I. The activation energies are increased for each circuit element upon reoxidation, indicating a net increase in the resistance for each component.

B. Analytical electron microscopy studies

Figure 4(a) shows a low-magnification bright-field TEM micrograph of $BaTiO_3$ dielectric in the as-cofired (without reoxidation) capacitors. Structural defects, such as dislocation loops that are noted by the arrows, are frequently observed in the $BaTiO_3$ grains. The distribution of defects is, however, inhomogeneous throughout the dielectric layers. It is likely that the dislocation loops are created by clustering of vacancies since high densities of loops were also reported in $BaTiO_3$ processed in reducing atmospheres, particularly in regions without amphoteric dopants.[29,30]

TABLE I. Activation energies of electrode interfaces, grain boundaries, and dielectrics in Ni-$BaTiO_3$ MLCCs in different process states.

	E_A (eV)		
Capacitors	Electrode	Grain boundary	Grain
Co-fired	1.42±0.01	1.27±0.01	1.20±0.03
As-produced	1.45±0.02	1.30±0.02	1.21±0.03

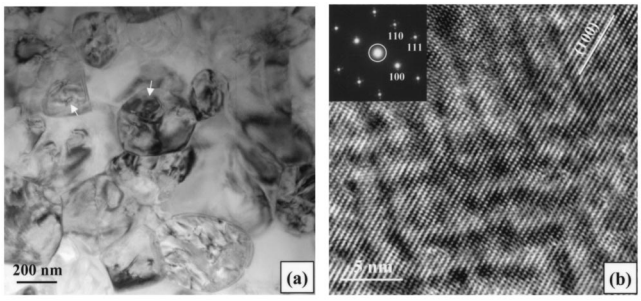

FIG. 4. Microstructure of the $BaTiO_3$ grains in the cofired capacitor. (a) Bright-field TEM image showing linear defects. (b) High-resolution TEM image presents modulated defect structures.

In addition to the linear defects evident in Fig. 4(a), modulated defect structures are also found occasionally in $BaTiO_3$ grains in the cofired capacitors when the grain is oriented in the $\langle 110 \rangle$ direction relative to the electron beam. Figure 4(b) shows a high-resolution TEM image of the modulated structure in $BaTiO_3$. The corresponding electron diffraction pattern inserted in the image shows incommensurate satellite spots present in addition to the basic reflections of the pseudocubic perovskite. The electron diffraction pattern is indexed as the $[10\bar{1}]$ zone axis of pseudocubic perovskite. The periodic image contrast superimposed on the basic lattice image of the $BaTiO_3$ is associated with structural modulations on the {111} plane of the $BaTiO_3$ crystal.[31] The formation of the modulated structure is associated with oxygen vacancies clustering on {111} planes in the frame work of the $BaTiO_3$ lattice. Part II discusses this type of phenomenon in greater detail.[8]

The distribution of oxygen nonstoichiometry in the dielectric layers is systematically studied using EELS. Shown in Fig. 5(a) is a bright-field image of $BaTiO_3$ grains adjacent to a Ni internal electrode in a cofired capacitor. The series of EEL spectra is obtained from positions numbered as 1–10 in grains 1–3. The fine structures of the Ti $L_{2,3}$ and O *K* edges vary as a function of distance from the Ni electrode; selected spectra are shown in Fig. 5(b) to highlight the changes. The lowest energy peak is the Ti L_3 edge (initial state $2p_{3/2}$) and the next is the Ti L_2 edge (initial state $2p_{1/2}$). The oxygen K edge contains a series of peaks labeled as *A*–*D*.[32,33] In the spectra obtained closest to the electrodes 1–3 ($p1$–$p3$) within grain 1 (G1), the L_3 edges are not split and the peak intensities of the O *K* edges are relatively low. These edge characteristics indicate higher concentrations of oxygen vacancies in $BaTiO_3$.[31,34] Splitting of the Ti L_3 edges is observed in spectra taken farther away from the electrode interface ($p4$–$p10$), which indicates the e_g-t_{2g} splitting that arises through orbital interactions between the Ti 3*d* and oxygen atoms. The relative intensity of the peak *A* under the O *K* edges also increase away from the interface. In general

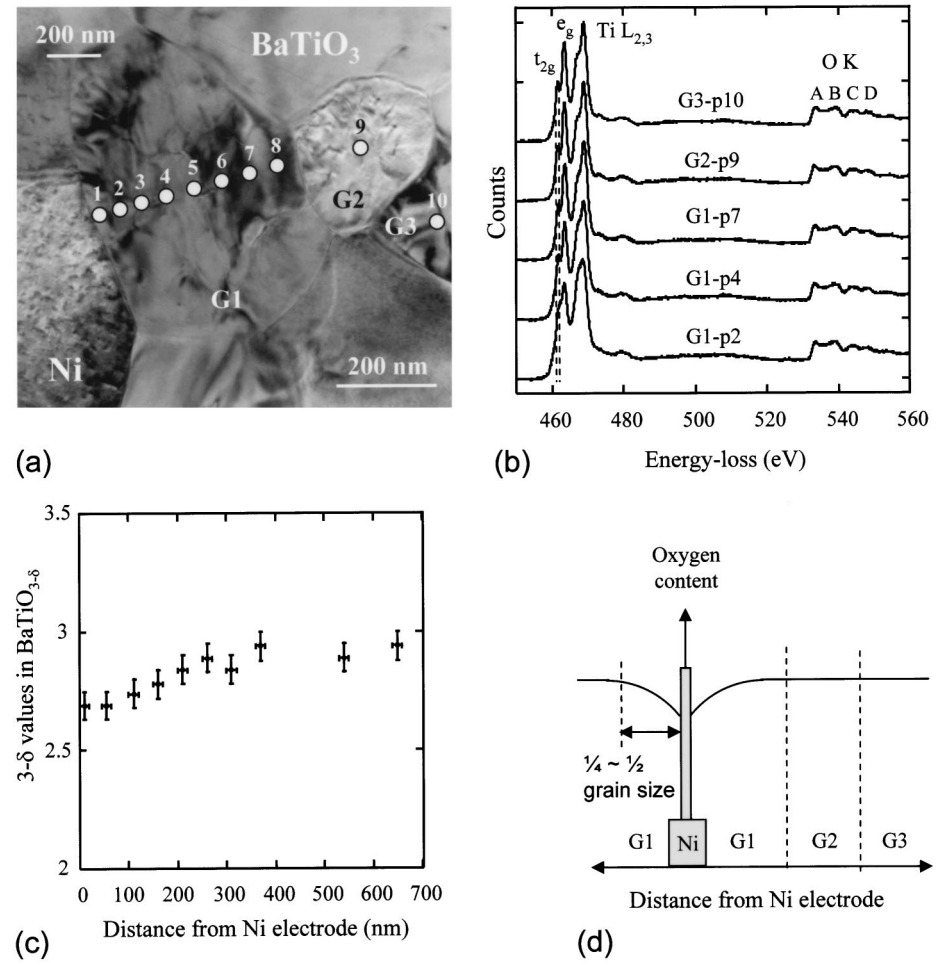

FIG. 5. (a) Bright-field image of the cofired capacitor showing Ni internal electrode and $BaTiO_3$ grains where series EELS spectra are obtained. (b) Fine structures of Ti $L_{2,3}$ and O K edges at different positions. (c) Variation of oxygen content as a function of the distance from the Ni electrode. (d) Schematic presentation of oxygen content in $BaTiO_3$ grains as a function of the distance to the internal Ni electrodes.

fine structures of the Ti $L_{2,3}$ and O K edges are quite similar from spectrum $p6$ to spectrum $p10$, implying the oxidation states and stoichiometry of the $BaTiO_3$ also similar. The spectra obtained from positions 1 to 3 ($p1-p3$) correspond to the case where e_g and t_{2g} bands may overlap and spectra from positions 4 to 10 ($p4-p10$) correspond to the case where a gap of e_g and t_{2g} exists.[35]

The oxygen content of $BaTiO_3$ is quantified using a K-factor (or sensitivity factor) approach.[36] This method is explained in a previous paper, in which an EELS spectrum obtained from an air-processed $BaTiO_3$, which is believed to be fully stoichiometric, is used as a standard.[31] The calculated stoichiometry, i.e., the values of $3-\delta$ in the formula $BaTiO_{3-\delta}$, as a function of distance from the Ni electrode is shown in Fig. 5(c). The lowest oxygen content is found in the grain region near the Ni electrode and the oxygen content increases gradually away from the Ni electrode. Eventually, the oxygen concentration in the $BaTiO_3$ lattice becomes uniform and close to the stoichiometric oxide values when the distance from the electrode is larger than 0.5 μm.

The nonstoichiometry in the reduced $BaTiO_{3-\delta}$ perovskite is accommodated by the valence decrease of the Ti ions. In Fig. 5(b) the EEL spectra are aligned at the onset of the O K edge (532 eV). A relative shift of the Ti L_3 edge of about 0.7 eV down in energy, as indicated by the dashed lines, is observed from spectrum $p2$ to spectrum $p7$, implying a lower oxidation state of Ti in the regions near the electrode. Additionally, the shift of the edge onset to lower energies may be associated with a reduction of the band gap of dielectric upon reduction.[37]

EELS analysis of this type has been performed on more than five similar regions in the cofired capacitors near the Ni electrodes and similar trends are observed. In general, the oxygen concentration in $BaTiO_{3-\delta}$ varies as a function of the distance from the internal Ni electrode, as schematically presented in Fig. 5(d), although the absolute values of stoichiometry vary slightly. We hypothesize that this local phenomenon is due to oxygen loss resulting from the decomposition of organic binders in the Ni paste. There are many complex steps involved in the decomposition of the organic materials used as binder plasticizers and dispersants.[38,39] Organics used in the thick film electrode paste are often difficult to remove, and could lead to residual graphitic carbon. Then at higher temperature an additional reaction involving the oxidation of the carbon is at the expense of oxygen from the perovskite lattice, particularly close to the electrodes since a series of reactions qualitatively accounts for the inhomoge-

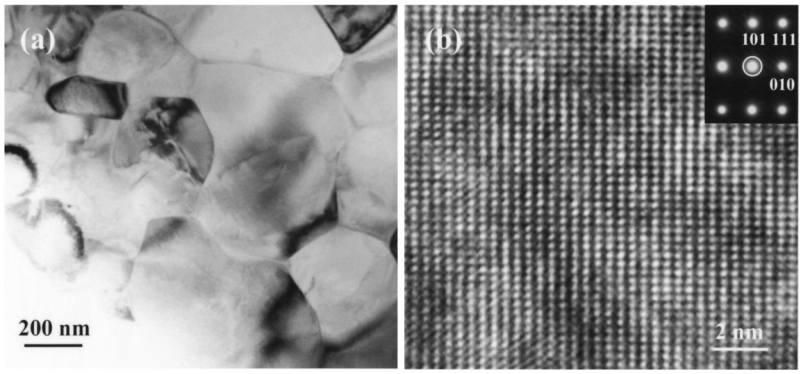

FIG. 6. Microstructure of $BaTiO_3$ grains in the as-produced capacitor. (a) Bright-field TEM image showing a few linear defects. (b) High-resolution TEM image presents a regular perovskite structure.

neity in the nonequilibrium oxygen distributions in the $BaTiO_3$ layers under cofiring conditions in the commercial MLCCs.

Figures 6(a) and 6(b) show conventional and high-resolution TEM images of the $BaTiO_3$ after reoxidation of the MLCC (as-produced). Only a few structural defects are present in Fig. 6(a). Compared with the microstructure of $BaTiO_3$ in the cofired capacitors in Fig. 4(a), the density of the structural defects is much lower in the $BaTiO_3$ dielectric layers. This is realized by the significant decrease in oxygen vacancies through the reoxidation treatment. Figure 6(b) shows a high-resolution TEM image of a $BaTiO_3$ grain in the as-produced (reoxidized) capacitors. Image contrast associated with structural modulations is not observed in any grains.

The analysis of oxygen content in $BaTiO_3$ layers is also carried out in the as-produced (reoxidized) capacitors using EELS. The region of interest for EELS analysis is shown in the bright-field TEM image of Fig. 7(a), where a Ni electrode and adjacent $BaTiO_3$ grains are shown. The EEL spectra are taken from the regions noted by $p1-p7$ within individual $BaTiO_3$ grain, and selected spectra (spectra $p1$, $p4$, and $p6$) are shown in Fig. 7(b). The splitting of the Ti L_3 edges is observed in all spectra and no apparent chemical shifts are observed in any spectra. The stoichiometry of the barium titanate is plotted Fig. 7(c). It is clear that reoxidation significantly improves the homogeneity in oxygen distribution through the $BaTiO_3$ layers.

Figure 8(a) is a schematic representation of oxygen content in the as-produced (reixuduzed) capacitors based on similar EELS analysis on more than five regions. In general, the oxygen content is more homogeneous as compared to the cofired capacitors. The homogeneity in the oxygen concentration results in a significant improvement in insulation resistance of the capacitors [see Fig. 2(a)] due to the increase in oxygen content in the $BaTiO_3$ grains that are in contact with Ni electrodes. However, the SEM-VC (Ref. 40) image shown in Fig. 8(b) indicates that on a larger length scale the distribution of the oxygen vacancies is inhomogeneous in the as-produced capacitors with an accumulation of oxygen vacancies near the electrode terminations. A stronger dependence of the image contrast with respect to applied dc potential is observed near the tips of the Ni electrodes. This dependence is an indication of conduction associated with a

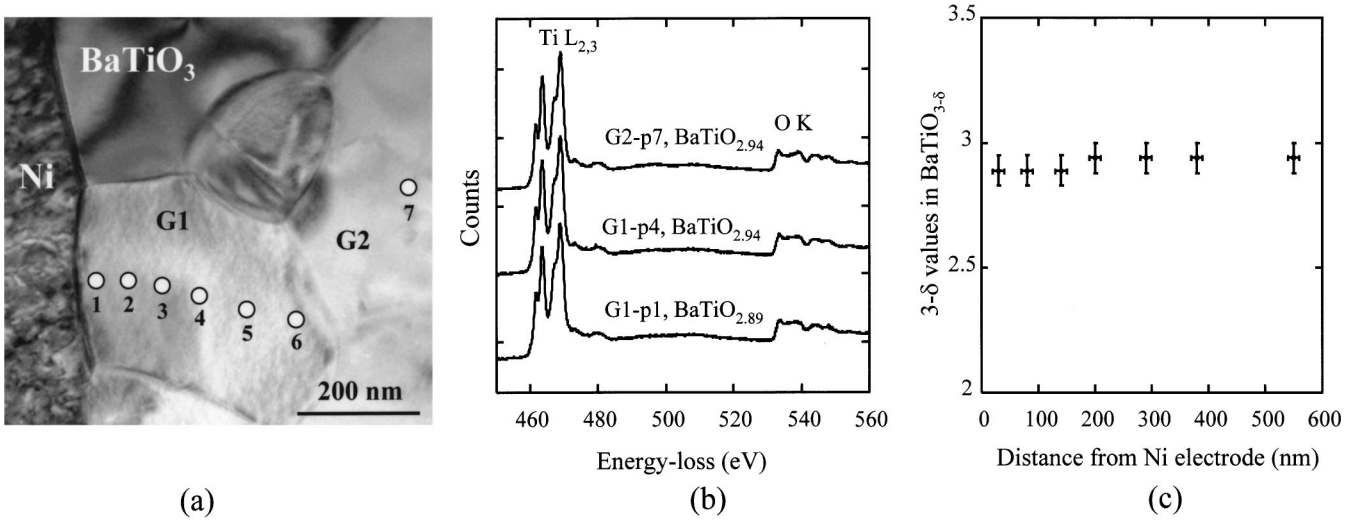

FIG. 7. (a) Bright-field image of the as-produced capacitors showing the Ni internal electrode and $BaTiO_3$ grains where series EELS spectra were taken. (b) Fine structures of Ti $L_{2,3}$ and O K edges at different positions showing almost identical peak shapes. (c) The variation of oxygen content as a function of the distance from Ni electrode.

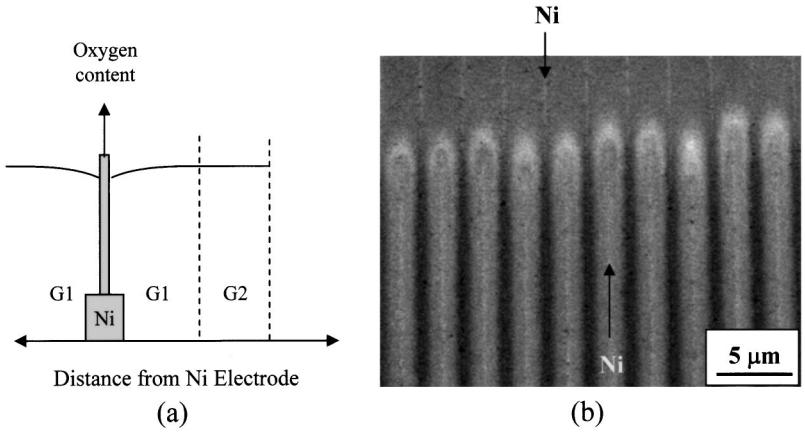

FIG. 8. (a) Schematic presentation of oxygen concentration in the $BaTiO_3$ active layer of as-produced MLCC. (b) SEM-VC image showing a high concentration of oxygen vacancies at the ends of Ni electrodes in the as-produced MLCC.

relatively high local concentration of oxygen vacancies.[26,35] The concentration of oxygen vacancies near the tips of the electrodes is much higher than that within the dielectric layers, leading to local high conductivity.

Figure 9 shows a model for oxygen diffusion into the multilayer device during the reoxidation process. This proposed model is based on the evidence shown in Figs. 5, 7, and 8, and earlier studies using oxygen (O^{18}) radioactive tracers.[41] Since Ni-$BaTiO_3$ MLCCs are cofired at ~1300 °C in a P_{O_2} of $\sim 10^{-10}$ atm, under this reducing ambient, it is believed that some oxygen vacancies result from

$$O_O \rightarrow \tfrac{1}{2}O_2 + V_{\ddot{O}} + 2e' \tag{3}$$

However, it is clear that a much more harsh reduction may be associated with residual carbon from the debinding process of organic components of the Ni paste. Therefore, along with the creation of oxygen vacancies during cofiring, two electrons in the conduction band will be activated, which results in a lower insulation resistance of the capacitor. During reoxidation annealing at lower temperature and higher oxygen partial pressure (800 °C, P_{O_2} of $\sim 10^{-8}$ atm), oxygen diffuses into the devices from the margins of Ni-$BaTiO_3$ MLCCs and goes into $BaTiO_3$ dielectric layers along the Ni-$BaTiO_3$ interfaces. The concentration of oxygen vacancies and compensation electrons in $BaTiO_3$ dielectric layers are decreased. Consequently, the insulation resistance of each circuit element is significantly increased. However, high concentrations of oxygen vacancies are observed near the tips of the electrodes. The local phenomenon may be associated with nonequilibrium of oxygen distribution under process conditions of commercial devices. These are anticipated to be weak areas for the degradation in insulation resistance of the Ni-$BaTiO_3$ MLCCs that may have less reoxidation than other areas.[16,31]

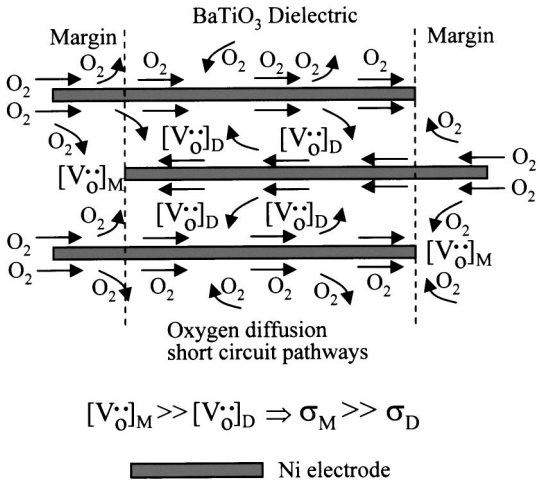

FIG. 9. A proposed model for oxygen diffusion path way into the multilayer device during reoxidation process. V_M^{**}: vacancy concentration in margin regime, V_D^{**}: vacancy concentration in dielectric layer.

IV. CONCLUSIONS

In this work we study the dielectric and microstructural evolution of *n*-type Ni-$BaTiO_3$ BME multilayer ceramic capacitors through commercial processing stages. IS shows that the internal interfaces, including $BaTiO_3$ grain boundaries and electrode interfaces, play key roles in the electrical performance of the devices. The insulation resistance of the MLCC is significantly improved by the reoxidation process. TEM coupled with EELS provides insight into the reoxidation process. High densities of structural defects in the cofired $BaTiO_3$ grains are correlated with aggregates of oxygen vacancies. In some cases the reduction can produce modulated defect structures within the $BaTiO_3$ lattice. Furthermore, in the cofired capacitors, the oxygen distribution is highly inhomogeneous across the dielectric layers. The lowest oxygen content is found in the regions near Ni electrodes. In the reoxidized (as-produced) capacitors, only a few structural defects are present in $BaTiO_3$ grains. The enhancement in insulation resistance of the capacitors is associated with lower concentration of oxygen vacancies and their associated structural defects. In addition, oxygen vacancy concentration gradients in the $BaTiO_3$ layers are mostly homogenized and are uniform throughout the active areas of MLCCs.

ACKNOWLEDGMENTS

This work has been supported in part by the NSF-I/UCRO Center for Dielectrics Studies (CDS) and KEMET Electronic Corporation. We also thank CDS members for

useful discussions and Materials Research Institute TEM facilities at the Pennsylvania State University, University Park.

[1]J. M. Herbert, *Ceramic Dielectrics and Capacitors* (Gordon and Breach, Philadelphia, 1985).
[2]H. Chazono and H. Kishi, Jpn. J. Appl. Phys., Part 1 **40**, 5624 (2001).
[3]H. Kishi, Y. Mizuno, and H. Chazono, Jpn. J. Appl. Phys., Part 1 **42**, 1 (2003).
[4]R. Waser, J. Am. Ceram. Soc. **72**, 2234 (1989).
[5]R. Waser, T. Baiatu, and K. H. Härdtl, J. Am. Ceram. Soc. **73**, 1645 (1990).
[6]R. Waser, T. Baiatu, and K. H. Härdtl, J. Am. Ceram. Soc. **73**, 1654 (1990).
[7]T. Baiatu, R. Waser, and K. H. Härdtl, J. Am. Ceram. Soc. **73**, 1663 (1990).
[8]G. Y. Yang, G. D. Lian, E. C. Dickey, C. A. Randall, D. E. Barber, P. Pinceloup, M. A. Henderson, R. A. Hill, J. J. Beeson, and D. J. Skamser,J. Appl. Phys. **96**, 7500 (2004).
[9]J. R. Macdonald and W. B. Johnson, in *Impedance Spectroscopy Emphasizing Solid Materials and Systems*, edited by J. R. Macdonald (Wiley, New York, 1987).
[10]D. C. Sinclair and A. R. West, J. Appl. Phys. **66**, 3850 (1989).
[11]A. R. West, D. C. Sinclair, and N. Hirose, J. Electroceram. **1**, 65 (1997).
[12]H. S. Maiti and R. N. Basu, Mater. Res. Bull. **21**, 1107 (1986).
[13]H. Chazono and H. Kishi, J. Am. Ceram. Soc. **83**, 101 (2000).
[14]S. H. Yoon, J. H. Lee, and D. Y. Kim, J. Am. Ceram. Soc. **85**, 3111 (2002).
[15]C. A. Randall, S. F. Wang, D. Laubscher, J. P. Dougherty, and W. Huebner, J. Mater. Res. **8**, 871 (1993).
[16]H. Chazono and H. Kishi, Jpn. J. Appl. Phys., Part 1 **40**, 5624 (2001).
[17]M. Vollman and R. Waser, J. Am. Ceram. Soc. **77**, 235 (1994).
[18]J. E. Clayton, G. Y. Yang, E. Furman, D. Martin, E. C. Dickey, and C. A. Randall, J. Electroceram. (to be published).
[19]C. H. Lai and T. Y. Tseng, J. Am. Ceram. Soc. **77**, 2419 (1994).
[20]H. M. Al-Allak, A. W. Brinkman, G. J. Russell, and J. Woods, J. Appl. Phys. **63**, 4530 (1988).
[21]D. Y. Wang and K. Umeya, J. Am. Ceram. Soc. **73**, 669 (1990).
[22]A. Bar-Lev, *Semiconductors and Electronic Devices* (Prentice-Hall International, Inc., London, 1979).
[23]K. Hayashi, T. Yamamoto, Y. Ikuhara, and T. Sakuma, J. Am. Ceram. Soc. **83**, 2684 (2000).
[24]Y. Tsur, T. D. Dunbar, and C. A. Randall, J. Electroceram. **7**, 25 (2001).
[25]N. Szydlo and R. Poirer, J. Appl. Phys. **51**, 3310 (1980).
[26]D. P. Cann and C. A. Randall, J. Appl. Phys. **80**, 1628 (1996).
[27]E. H. Rhoderick and R. H. Williams, *Metal-semiconductor Contact*, 2nd ed. (Clarendon Press, Oxford, 1988).
[28]S. M. Sze, *Physics of Semiconductor Devices*, 2nd ed. (Wiley, New York, 1981).
[29]C. Metzmacher and K. Albertsen, J. Am. Ceram. Soc. **84**, 821 (2001).
[30]M. Shiojiri, T. Isshiki, H. Saijo, M. Tsujikura, A. Nakada, Y. Nakano, M. Ikeda, and T. Nomura, Phys. Status Solidi A **129**, 353 (1992).
[31]G. Y. Yang, E. C. Dickey, C. A. Randall, M. S. Randall, and L. A. Mann, J. Appl. Phys. **94**, 5990 (2003).
[32]N. D. Browning, D. J. Wallis, P. D. Nellist, and S. J. Pennycook, Micron **28**, 334 (1997).
[33]L. A. Grunes, R. D. Leapman, C. N. Wilker, R. Hoffmann, and A. B. Kunz, Phys. Rev. B **25**, 7157 (1982).
[34]R. F. Klie and N. D. Browning, Appl. Phys. Lett. **77**, 3737 (2000).
[35]J. K. Burdett, *Chemical Bonding in Solids* (Oxford University Press, New York, 1995).
[36]D. C. Joy, A. D. Romig, and J. I. Goldstein, *Principles of Analytical Electron Microscopy* (Plenum, New York, 1986).
[37]R. Brydson, H. Sauer, and W. Engel, in *Transmission Electron Energy Loss Spectroscopy in Materials Science*, edited by M. M. Disko, C. C. Ahn, and B. Fultz, (Warrendale, Pennsylvania, 1991), pp. 131–154.
[38]H. T. Kim, J. H. Adair, and M. T. Lanagan, Am. Ceram. Soc. Bull. **80**, 34 (2001).
[39]J. A. Lewis, Annu. Rev. Mater. Sci. **27**, 147 (1997).
[40]D. E. Newbury, D. C. Joy, P. Echlin, C. E. Fiori, and J. I. Goldstein, *Advanced Scanning Electron Microscopy and X-Ray Microanalysis* (Plenum, New York, 1986).
[41]M. Opitz, J. Roubert, K. Albertson, D. Hennings, J. Beeson, and C. A. Randall, J. Am. Ceram. Soc. **86**, 1879 (2003).